Fast semi-analytical acoustic inversion for quantitative optoacoustic tomography

Amir Rosenthal, Thomas Jetzfellner, Daniel Razansky, and Vasilis Ntziachristos
Institute for Biological and Medical Imaging, & Chair for Biological Imaging Technische Universität of München and Helmholtz Zentrum München, Ingolstädter Landstraβe 1, 85764 Neuherberg, Germany

ABSTRACT

We present a fast inversion algorithm for quantitative two- and three-dimensional optoacoustic tomography. The algorithm is based on an accurate and efficient forward model, which eliminates the need for regularization in the inversion and can achieve real-time performance. The reconstruction speed and other algorithmic performances are demonstrated using numerical simulation studies and experimentally on tissue-mimicking optically heterogeneous phantoms and small animals. In the experimental examples, the model-based reconstructions manifested correctly the effect of light attenuation through the objects and did not suffer from the artifacts which usually afflict the commonly used filtered backprojection algorithms, such as negative absorption values.

Keywords: imaging, inverse problems, optoacoustics, photoacoustics, tomography.

1. INTRODUCTION

Optoacoustic tomography (OAT) is a non-invasive imaging method for high-resolution mapping of optical absorption in tissues[1-4]. The technique is based on illuminating the region of interest with short high-power laser pulses, which create an instantaneous temperature elevation and a per-pulse thermal expansion within it. In response, high-frequency acoustic waves are generated owing to thermo-elastic expansion, which are then recorded and used for image reconstruction using different inversion algorithms[5-8]. The ability of OAT to image tissue has been shown by visualizing vascular anatomy[2], tumor angiogenesis[9], as well as functional imaging of blood oxygenation[10] in living tissues of small animals and humans. Although absorbing substances such as blood naturally manifest high optoacoustic contrast, it was recently demonstrated that the technique can effectively visualize tissues and organisms that contain no hemoglobin contrast[11] or contain externally generated contrast, e.g. using dyes[4] or light-absorbing nanoparticles[12] . It has been also shown that common fluorochromes, such as fluorescent proteins or fluorescent molecular probes can be resolved with high specificity when employing illumination at several optical wavelengths using multispectral optoacoustic tomography (MSOT) [4,13].

Back-projection algorithms have been widely used for volumetric image reconstruction in OAT applications[5,6,14]. These algorithms are based on closed-form inversion formulas expressed in two or three dimensions and are analogues to the Radon transform. Back-projection formulas exist for several detection geometries and are implemented either in the spatio-temporal domain[6,14] or in the Fourier domain[5]. A disadvantage of conventional back-projection algorithms is that they are not exact[6] and may lead to the appearance of substantial artifacts in the reconstructed images. A common artifact is the accentuation of fast variations in the image (small details), which is accompanied by negative optical-absorption values that otherwise have no physical interpretation. Although these artifacts have not prevented the use of back-projection algorithms for structural imaging[2], they can significantly limit the quantification capacity, the image fidelity, and the accurate use of the method for functional and molecular imaging applications[13], including multi-spectral imaging applications, since these imaging modes require high quantification ability. In addition, back-projection algorithms are based on an ideal description of the acoustic wave propagation and detection as well as on specific

Photons Plus Ultrasound: Imaging and Sensing 2011, edited by Alexander A. Oraevsky, Lihong V. Wang,
Proc. of SPIE Vol. 7899, 78992R · © 2011 SPIE · CCC code: 1605-7422/11/$18 · doi: 10.1117/12.874048

detection geometries, therefore they cannot be easily generalized into a more realistic optoacoustic illumination-detection models that incorporate configuration and instrumentation-dependent factors.

In this work we suggest a novel semi-analytical model-based inversion scheme for quantitative optoacoustic image reconstruction, termed interpolated-matrix-model inversion (IMMI). In contrast to backprojection algorithms, the model-based scheme is not based on an analytical solution to the inverse problem. Instead, a solution to the forward problem is used to obtain the OAT image by minimizing the mean square error between the measured acoustic signals and those which correspond to the optimized OAT image. Ideally, this approach can yield artifact-free quantified OAT reconstructions. However, the computational complexity involved with previously suggested model-based approaches, which used finite-element-based and other computationally intensive or inaccurate numerical solutions to the acoustic propagation problem[7,8] has so far limited the spatial resolution achieved and therefore hindered their effective implementation. The semi-analytical solution presented in this paper is exact for piecewise planar acoustic-source functions, which significantly improves the accuracy and computational speed. In addition, IMMI requires solving the forward acoustic problem only once, thus reducing the overall computational complexity. The solution is saved in a matrix, which is inverted in order to reconstruct the image. The inverted matrix does not depend on the data. Thus, the same inverse matrix may be used for different experimental data obtained by the same system. If the inverse matrix of the system has been calculated beforehand, the reconstruction may be performed in real time.

We demonstrate the performance of the method on both numerical data as well as experimental data obtained for optically heterogeneous tissue mimicking phantoms. In addition, the algorithm was tested ex-vivo for imaging the brain of a mouse head. Our results demonstrate that the proposed algorithm renders high-resolution high-quality optoacoustic images, which do not suffer from back-projection-related reconstruction artifacts and leads to better presentation of anatomical features in small-animal imaging.

2. THEORETICAL BACKGROUND

The forward problem in OAT is derived under the condition of thermal confinement, i.e. that the temperature increase in each part of the irradiated object is not affected by the temperature increase in neighboring regions, i.e. heat conductance is negligible. This condition is usually fulfilled for laser pulses with duration lower than 1 μsec[1] and guarantees that the acoustic sources created in the object are proportional to the absorbed optical energy. Under this condition, and neglecting acoustic losses, the propagation equation for the acoustic fields is given by[15]

$$\frac{\partial^2 p(r,t)}{\partial t^2} - c^2 \rho \nabla \cdot \left(\frac{1}{\rho} \nabla p(r,t) \right) = \Gamma \frac{\partial H(r,t)}{\partial t}, \tag{1}$$

where c and ρ are velocity of sound in tissue and its density, Γ is the Grüneisen parameter, and H is the amount of energy absorbed in the tissue per unit volume and per unit time. H can be represented as a product between its spatial and temporal components, i.e. $H(r,t) = H_r(r) H_t(t)$.

In our analysis we focus on propagation of acoustic fields in acoustically homogenous media. Then, Eq. 1 takes the form of

$$\frac{\partial^2 p(r,t)}{\partial t^2} - c^2\nabla^2 p(r,t) = \Gamma H_r(r)\frac{\partial H_t(t)}{\partial t}. \tag{2}$$

In most practical cases, the duration of the optical pulse is short enough to be approximated by a delta function, i.e. $H_t(t) = \delta(t)$. This simplification leads to an analytical solution for Eq.2, which is given by a Poisson-type integral[15]

$$p(r,t) = \frac{\Gamma}{4\pi c}\frac{\partial}{\partial t}\int_{R=ct}\frac{H_r(r')}{R}dA', \tag{3}$$

where $R = |r - r'|$ and the integration is performed over a sphere with a radius of $R = ct$. In a two-dimensional (2D) geometry, for which all the sources lie in a plane, the integration is performed over a circle. For a given sensor position $r = (x_0, y_0)$, the integral in Eq.3 can be explicitly rewritten as

$$\int_{R=ct}\frac{H_r(r')}{R}dA' = \int_{\theta_1}^{\theta_2} H_r(x_0 + R\cos\theta, y_0 + R\sin\theta)d\theta \quad . \tag{4}$$

In both 2D and 3D geometries, the calculation of Eq. 4 poses numerical difficulties that stem from the inconsistency of the grid with the surface on which the integral is to be calculated. Calculating the derivative of the integral only exacerbates the numerical problems. Typically, in order to accurately calculate Eq. 4, the resolution of the grid should be considerably higher than what otherwise be required to accurately represent $H_r(r)$. This results in computational inefficiency of the solution to the forward problem.

Inversion formulas to Eq. 3 exist for several geometries[6][6]. In 2D geometries, an exact inversion formula was developed for a circular scanning configuration[14]. The inversion formula required calculating a two dimensional integral over sum of an infinite function series. Due to numerical complexity of the calculation, a first order approximation is conventionally used instead[2,6,14]. The approximate solution is essentially the well-known modified back-projection formula given by[6]:

$$H_r(r) = \frac{-1}{2\pi c^2\Gamma}\int_{t=|R'-R|c}\frac{1}{t}\left[\frac{\partial p(r,t)}{\partial t} - \frac{p(r,t)}{t}\right]dA'. \tag{5}$$

Because of its simplicity, the modified back-projection formula has been widely used to reconstruct OAT images from acoustic measurement data. The experimental studies showed that even though Eq.5 is not exact, it is still very successful in detecting the position and shape of absorbing objects in turbid media[2]. However, as we show in the following, the reconstruction artifacts associated with the modified back-projection formula might significantly limit its use for quantitative image reconstruction purposes.

3. MODEL-BASED INVERSION

In this section we describe the IMMI algorithm. For clarity, we limit our discussion to the semi-analytical solution of Eq.3 in a 2D geometry. However, as shown in the following, the solutions can be easily generalized to 3D by summing the acoustic signals that originate at different planes. The solution is given by a matrix equation, which can be subsequently inverted.

We further define a grid to discretely represent $H_r(r)$ and mark the grid coordinates by r_i. In the forward problem, one seeks to find $p(r,t)$ given the OAT image on the discrete grid $H_r(r_i)$. In order to calculate the integral in Eq. (3), we interpolate $H_r(r_i)$ for coordinates which are not on the grid. The interpolated image can be represented as a superposition of the values of $H_r(r_i)$, i.e.

$$H_r(r) = \sum_{i=1}^{n} f_i(r_1,...,r_n,r) H_r(r_i) \quad , \tag{6}$$

where the functions $f_i(r_1,...,r_n,r)$ are determined by the type of interpolation used. Since we assume that the grid points are predetermined, the interpolation functions can be described solely as a function of r, namely $f_i(r)$. For most types of interpolations, the value of the function $H_r(r)$ depends only upon the value of $H_r(r_i)$ in neighboring point. Thus, for such local interpolations most of the elements in the sum in Eq. (6) are equal to zero. Substituting Eq. (6) into Eq. (3) and performing the integration on a circle instead of a sphere, one obtains

$$p(r,t) = \sum_{i=1}^{n} g_i(r,t) H_r(r_i) \quad , \tag{7}$$

where

$$g_i(r,t) = \frac{\Gamma}{4\pi c} \frac{\partial}{\partial t} \int_{R=ct} \frac{f_i(r')}{R} d\ell'. \tag{8}$$

For a local interpolation, the function $g_i(r,t,r')$ would be identically zero for most of the i indices, except for those which correspond to grid points in the neighborhood of the circle $R = ct$. We note that Eqs. (7)-(8) are also valid when the detector is not located in the plane of the acoustic sources. In that case, R should be replaced by $\sqrt{R^2 - h^2}$, where h is the distance of the sensor from the current reconstruction plane.

One crucial step in the algorithm is choosing the appropriate interpolation functions. The functions should be such that yield an analytical solution to the integral in Eq. (3). In addition, because of the derivative operator in Eq. (3), the interpolation functions should also be differentiable or piecewise differentiable. In this work a linear interpolation is used for which the resulting function $H_r(r)$ is piecewise planar. The interpolation is performed by tiling the x-y reconstruction plane with right-angle triangles with vertexes on the grid point as illustrated in Fig. 1. For each coordinate (x_i, y_i) we assign $H_r(r_i)$ as its elevation value on the z axis, i.e. $z_i = H_r(r_i)$. Accordingly, each triangle can be described by a set of the three coordinates of its vertices (x_ℓ, y_ℓ, z_ℓ), (x_n, y_n, z_n), and (x_m, y_m, z_m). The interpolated values of $H_r(r)$ within each triangle are thus taken as the value of the plane elevation calculated via

$$H_r(x,y) = -\frac{Ax + By + D}{C}, \tag{9}$$

where

$$A = \begin{vmatrix} 1 & y_\ell & z_\ell \\ 1 & y_n & z_n \\ 1 & y_m & z_m \end{vmatrix}, B = \begin{vmatrix} x_\ell & 1 & z_\ell \\ x_n & 1 & z_n \\ x_m & 1 & z_m \end{vmatrix}, C = \begin{vmatrix} x_\ell & y_\ell & 1 \\ x_n & y_n & 1 \\ x_m & y_m & 1 \end{vmatrix}, D = \begin{vmatrix} x_\ell & y_\ell & z_\ell \\ x_n & y_n & z_n \\ x_m & y_m & z_m \end{vmatrix} \tag{10}$$

and the operation $|\cdot|$ refers to matrix determinant. Because the coefficients A, B, and D are linearly dependant on z_ℓ, z_n, and z_m, the interpolation in Eq. (9) fulfills the condition in Eq. (6). Substituting Eq. (9) into Eq. (4), one obtains

$$\int_{R=ct} \frac{H_r(r')}{R} dA' = -C^{-1} \int_{\theta_1}^{\theta_2} [A(x_0 + R\cos\theta) + B(y_0 + R\sin\theta) + D] d\theta \quad . \tag{11}$$

The integral in Eq. (6) can then be solved analytically within each triangle resulting in a linear function of z_ℓ, z_n, and z_m. The coefficients of z_ℓ, z_n, and z_m are subsequently used to calculate $g_i(r,t)$ by substituting them into Eq. (11). We note that for a given grid coordinate with index i, the contribution to $g_i(r,t)$ generally originates from more than a single triangle.

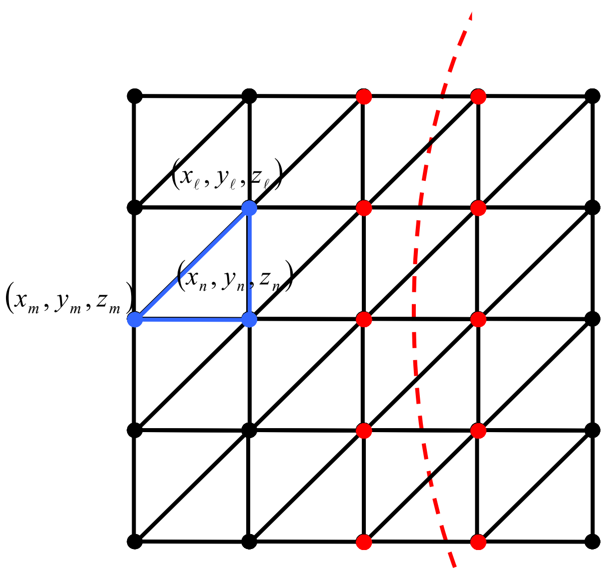

Fig. 1. A schematic description of grid upon which the OAT image is represented. Each grip point is assigned three coordinates. Each right-angle triangle represents a unit cell in which the image is interpolated linearly. The dotted red line represents a certain arc on which the integral in Eq. (4) is calculated, and the red grid points are the grid points that are involved in calculating the integral and correspond to the nonzero elements in Eq. (7).

In the next step, we define the spatial and temporal coordinates $\{(r_j, t_j)\}_j$ over which the acoustic signal is acquired. Denoting $p_{jk} = p(r_j, t_k)$, Eq. (7) can be written in a matrix form:

$$\mathbf{p} = \mathbf{Mz}, \tag{12}$$

where $\mathbf{p}$ is a column vector whose elements are p_{jk}, and $\mathbf{z}$ is a column vector whose element are z_i. The elements in the matrix $\mathbf{M}$ are the corresponding values of $g_i(r,t)$. For a given optoacoustic imaging system, the matrix $\mathbf{M}$ does not depend on the imaged object, but only on the image grid and the particular experimental tomographic acquisition geometry.

The inversion of the matrix relation in Eq. (12) is a standard problem in linear algebra, and can be performed in several ways. In this work, square error minimization is employed for inversion, i.e.

$$\mathbf{z}_{\text{sol}} = \arg\min_{Z} \|\mathbf{p} - \mathbf{Mz}\|^2, \tag{13}$$

where $\|\cdot\|$ is an ℓ_2 norm. Here the inversion is performed using the Moore-Penrose pseudo-inverse[16]:

$$\mathbf{z}_{\text{sol}} = \mathbf{M}^{\dagger}\mathbf{p}, \tag{14}$$

where $\mathbf{M}^{\dagger}$ is the pseudo-inverse and is given by $\mathbf{M}^{\dagger} = \left(\mathbf{M}^T\mathbf{M}\right)^{-1}\mathbf{M}^T$, and T denotes the conjugate transpose operator. The advantage of using the pseudo-inverse approach is that it is determined only by the experimental setup, e.g. sensors' positions with respect to center of rotation, sampling resolution etc., and not by the measured data. Thus, the pseudo-inverse $\mathbf{M}^{\dagger}$ can be calculated once for every measurement configuration with inversion reduced to multiplying it by the measured values of $\mathbf{p}$, a process that can be realistically performed in real time.

One of the advantages of IMMI is that many additional linear effects can be added to the model, while using the same inversion formula. In addition, unlike in the analytical inversion formulation, the position of the detectors is not restricted to specific geometries. In this work we have incorporated the frequency response of the transducer into the model. We define a matrix $\mathbf{F}$, which corresponds to the FFT operation on a 1D signal, i.e. $\mathbf{Fp}$ is the FFT of $\mathbf{p}$, and the diagonal matrix $\mathbf{G}$ whose elements correspond to the frequency response of the transducer. The subsequent forward problem becomes

$$\mathbf{p} = \mathbf{F}^{-1}\mathbf{GFMz} \tag{15}$$

with the inverse solution given by

$$\mathbf{z}_{\text{sol}} = \left(\mathbf{F}^{-1}\mathbf{GFM}\right)^{\dagger}\mathbf{p}. \tag{16}$$

4. EXPERIMENTAL RESULTS

We experimentally demonstrated our inversion method on tissue mimicking phantoms. The phantoms were measured in an OAT system similar to the one described in Ref. [3]. Briefly, a tunable OPO laser (MOPO-710, Spectra-Physics, Mountain View, CA, USA), providing <8 nsec duration pulses with 30 Hz repetition frequency in the visible spectrum (450–680 nm), was used in order to illuminate the sample under investigation. In all our experiments, we used a 650 nm wavelength at an average power of approximately 800 mW. In order to uniformly illuminate the phantoms imaged, the laser beam was expanded to about 2 cm and then split into two beams, illuminating the phantom from opposite sides. A custom made, cylindrically focused hydrophone (Precision Acoustics Ltd., Dorchester, UK; focal distance 40 mm) was used to record the optoacoustic signals emitted by the sample. For signal collection over 360o projections, the samples were rotated on a stage while the hydrophone was placed at a distance of 40 mm from the center of rotation. The full-width-at-half-maximum (FWHM) of the detector's frequency response was equal to 3.5 MHz, which corresponded to a spatial resolution of about 200 μm.

In the first set of experiments, we examined IMMI's ability to map light absorption changes caused by light attenuation in optically homogeneous turbid media. For that purpose, three phantoms with different absorption coefficients were used. The phantoms were cylindrically shaped and had a diameter of 16 mm and background reduced scattering coefficient of $\mu_s' = 10\,\mathrm{cm}^{-1}$. Cylindrical scattering and absorbing insertions with 8 mm diameter were introduced in the center of the three phantoms. The insertions had scattering similar to the background and optical absorption coefficients μ_a of 0.2 cm^{-1}, 0.5 cm^{-1}, and 1 cm^{-1}, respectively. The phantom surrounding the insertions was non-absorbing. The acoustic signals were measured over 360 degrees with increments of 3 degrees. All the reconstructions were performed over a 91×91 grid, which corresponded to a resolution of approximately 150 μm. The images of the phantom insertions were reconstructed using back-projection (Eq. (5)), as shown in Figs. 2a-c. Correction for the frequency response of the detector was obtained by deconvolving the measured acoustic signals from the impulse response of the detector. The reconstruction exhibited negative artifacts on the boundary of the phantom. In addition, only the boundary of the absorbing part of the phantom is visible, and the effect of light attenuation is not apparent. Figures 2 d-f show the corresponding reconstructions obtained using IMMI. In this case, we did not deconvolve the measured signals from the impulse response of the detector. Instead, the detector's response was taken into account in the forward acoustic model by way of Eq. (15). The figures clearly show that IMMI accurately captured the differences in light absorption due to the light attenuation changes as the value of the absorption coefficient in the insertion is increased. The run time for constructing and inverting the model matrix was approximately 30 minutes for the given experimental setup. After calculating the inverse matrix, recovery of an image for each experiment took only approximately 1.3 seconds. The inverse matrix's size was 8281×24120 elements and occupied approximately 3 GB of memory.

We note that in the IMMI reconstructions, the maximum values of the images are not obtained on the surface of the absorbing region, but rather deeper within the phantom. This effect is a result of out-of-plane signals that were detected by the transducer. Although the transducer is focused to a plane, the focal width depends on the acoustic frequencies measured and is proportional to the scale of the imaged objects. In addition, the scattering outer-boundary of the phantoms homogenizes the light fluence in the vertical direction, thus creating more out-of-plane acoustic signals. Figures 2g-i show simulated reconstruction results for the same phantoms. The light propagation in the plane was modeled using an analytical solution to the light diffusion equation with the appropriate parameters. Light distribution in the vertical direction was assumed to be Gaussian with a FWHM of 1 cm. The acoustic signals were calculated and used for the inversion. Although we used only a rough estimate for the light diffusion in the vertical direction, the simulated results closely resemble the measured ones.

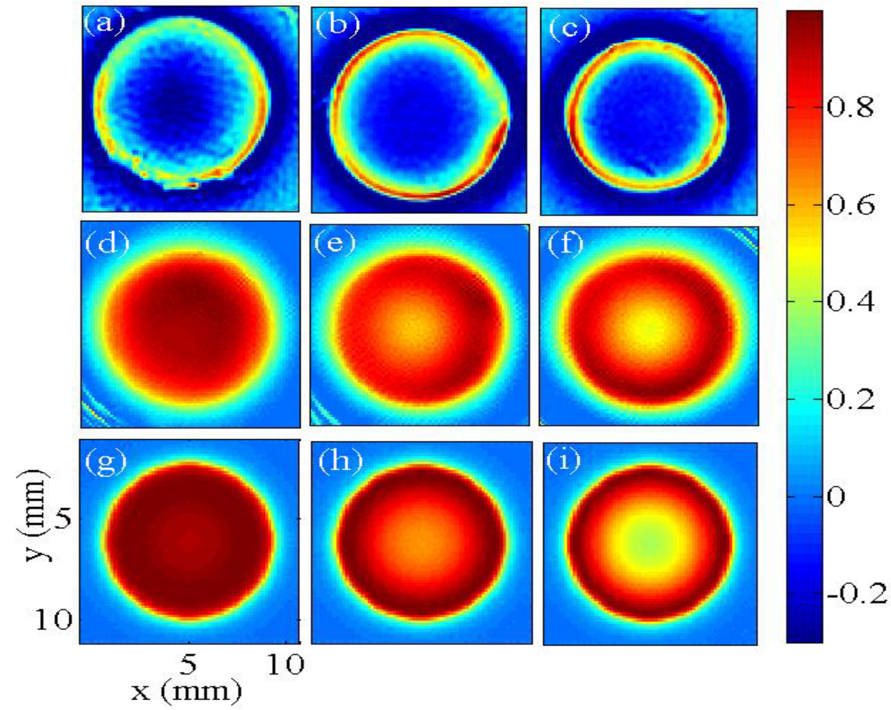

Fig. 2. Reconstructions of three homogeneous scattering and absorbing cylindrical insertions embedded in a purely scattering medium. The columns correspond to the following absorption coefficients: to 0.2 cm-1, 0.5 cm-1, and 1 cm-1, whereas the reduced scattering coefficient is 10 cm-1 for all the phantoms. The experinmental reconstructions obtained using the back-projection algorithm appear in the first row while the second row shows reconstructions obtained using the model-based inversion. Reconstructions based on the exact numerical simulations of the imaged configurations are shown in the third row.

To provide a better understanding on the performance of the model-based inversion in more complex environments, we prepared a set of heterogeneous tissue-mimicking phantoms. The phantoms were cylindrically shaped with a diameter of 16 mm. The bulk of the phantoms had an absorption coefficient of 0.2 cm^{-1}, whereas the insertions had an absorption coefficient of 1 cm^{-1}. The reduced scattering coefficient was kept at 10 cm^{-1}. The phantoms were scanned over 360 degrees with 2 degree increments. The reconstructions were performed on an 81×81 grid, which corresponded to a spatial resolution of about 200 µm. Photographs of the two phantoms are shown in Figs. 3a and 3d. The reconstructions obtained by the model-based inversions are shown in Figs. 3b and 3e, whereas the reconstructions obtained by the back-projection algorithm are shown in Figs. 3c and 3f. Similar effects are observed for both phantoms. The light attenuation is clearly visible in the model-based reconstructions, whereas, as expected, only the boundary of the phantoms and insertions are visible in the back-projection-based reconstructions. Therefore, IMMI more accurately reconstructs the underlying coupled absorption contrast and light attenuation, even though the results of the back-projection algorithm appear more visually pleasing. The run time for constructing and inverting the model matrix was approximately one hour. After calculating the inverse, the recovery of each image took only 1.6 seconds. The inverse matrix's dimensions were 6561×34740 and the matrix occupied approximately 3.6 GB of memory.

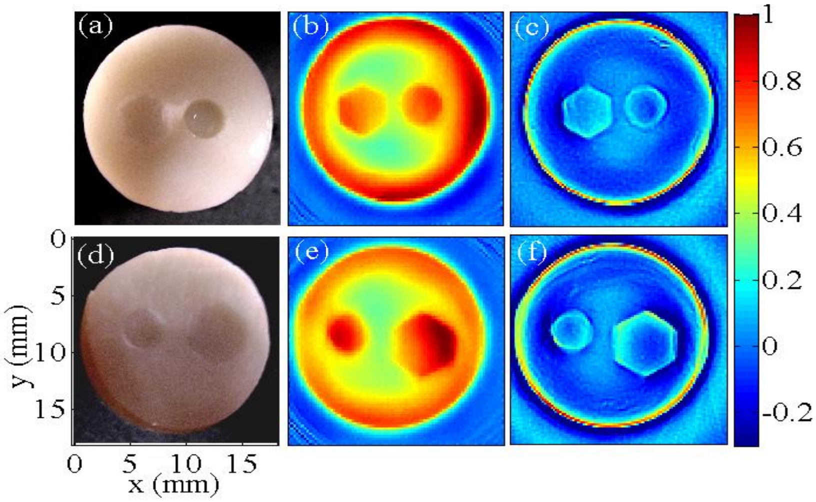

Fig. 3. Experimental reconstruction of two phantoms with insertions. The phantoms are shown in the first column; the model-based reconstruction is shown in the second column; and the back-projection reconstruction is shown in the third column.

To further demonstrate the abilities of IMMI, we tested in ex-vivo imaging of a mouse head. To increase the imaging resolution, the acoustic transducer used in the phantom experiments was replaced with one having a 7.5MHz central frequency (Model V320, Panametrics-NDT, Waltam, MA). The images reconstructed using the back-projection algorithm and IMMI are shown in Figs. 4a and 4b, respectively, and are compared to a photograph of a cryoslice at the same plane shown in Fig. 4c. The arrows in the images point to the eye sockets of the mouse. For both reconstructions, the image resolution was approximately 65 µm. Similarly to the phantom results, the image obtained by IMMI showed no negative artifacts and exhibited low-frequency image components. As a result, the anatomical features are better observed in the IMMI reconstruction; specifically, the boundary of the head and the eye sockets.

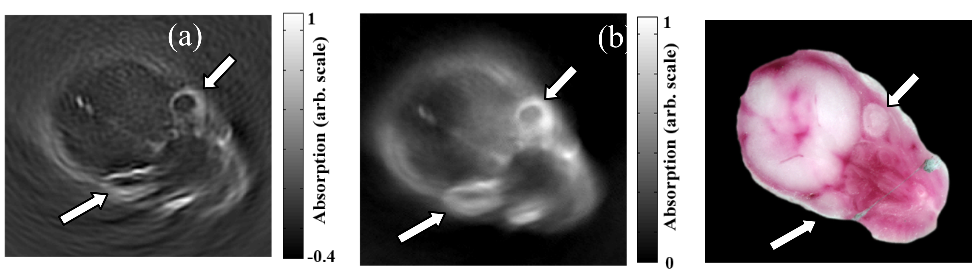

Fig. 4. Experimental reconstruction of a mouse head using (a) the back-projection algorithm and (b) IMMI. (c) a photograph of the corresponding cryoslice. The arrows in the images point to the mouse's eye sockets.

5. DISCUSSION

In this work, we have presented IMMI, a novel quantitative acoustic-inversion method for optoacoustic tomography (OAT). The method is based on modeling the forward problem using a semi-analytical solution to the acoustic-propagation equation. The solution is exact when the OAT image is a piecewise linear function. Using this solution, the measured acoustic fields can be represented as a linear combination of the values of the OAT image on the grid. Thus, a matrix relation has been formed between the measured acoustic signals and the desired image. By inverting the matrix relation, the OAT image can be recovered.

The method was successfully tested and compared to the commonly used back-projection algorithm on experimental data from tissue-mimicking phantoms and a mouse head. Two sets of tissue mimicking phantoms were used. In the first set, homogenous phantoms with increasing absorption coefficients were used. As a result of higher light attenuation, the acoustic signals from the middle of the phantoms were weaker as the absorption coefficient was increased. Accordingly, in the IMMI reconstruction we obtained that, as the absorption coefficient increased, the image became more biased toward the boundary, similarly to the results of exact numerical simulations using simulated optical properties. In contrast, the back-projection reconstructions were always biased towards the boundaries and did not change significantly as the absorption coefficient increased. The second set of phantoms included insertions with higher absorption than the background. For these phantoms, the model-based inversion managed to recover both the shape of the insertions and the expected light attenuation. Accordingly, insertions which were closer to the boundary received higher values in the recovered image. Several physically incorrect effects were observed in the back-projection reconstructions that also revealed the boundaries of the phantom and the insertions. Similar results were obtained for the mouse head images. Specifically, the back-projection reconstruction suffered from negative artifacts, excessive texture, and exhibited no low-frequency components. The IMMI-reconstructed images did not suffer from these afflictions and exhibited better visual quality, which eased the identification of anatomical features such as the eye sockets.

IMMI comes with several advantages over back-projection algorithms. First, it eliminates image artifacts associated with the approximated back-projection formulations, i.e. no negative absorption values are produced and the reconstructed image corresponds to the true light attenuation and energy deposition within the object. Clearly, since back-projection falsely emphasizes edges and fast image variations by producing large negative overshoots, it is capable of producing "good looking" high-contrast images. However, due to its approximate formulation, it fails to reproduce the correct and quantitative image of the actual laser energy deposition in tissue and the underlining optical absorption values. This property is especially important for quantitative imaging applications, i.e. molecular imaging studies, in which obtaining the correct absorption maps is of high importance. Similarly, IMMI is of significant importance in multi-spectral optoacoustic tomography MSOT applications[13] where accurate reconstructions are required for images obtained at different wavelengths in order to yield high performance visualization of chromophores with various spectral signatures distributed in tissue. Secondly, our model-based framework offers a generalization of the forward solution to more comprehensive acoustic propagation models without changing the inversion procedure. In this work, we only incorporated the frequency response of the acoustic detector into the model. However, additional linear effects, such as the frequency dependant acoustic attenuation and the detector's focusing characteristics can also be seamlessly and rigorously incorporated into the model. Finally and importantly, the model-based inversion can be adapted to any detection geometry.

REFERENCES

[1] Kruger R. A., Liu P., Fang Y. R., and Appledorn C. R., "Photoacoustic ultrasound (PAUS)--reconstruction tomography," Med Phys. 22, 1605-1609 (1995).

[2] Wang X., Pang Y., Ku G., Xie X., Stoica G., and Wang L. H. V., "Noninvasive laser-induced photoacoustic tomography for structural and functional in vivo imaging of the brain," Nat. Biotechnol. 21, 803-806 (2003).

[3] Razansky D. and Ntziachristos V., "Hybrid photoacoustic molecular tomography using finite-element-based inversion," Med. Phys. 34, 4293–4301 (2007).

[4] Razansky D., Vinegoni C., and Ntziachristos V., "Multispectral photoacoustic imaging of fluorochromes in small animals", 32(19), 2891-2893 (2007).

[5] Koestli K., Frenz M., Bebie H., and Weber H., "Temporal backward projection of optoacoustic pressure transients using Fourier transform methods," Phys. Med. Biol. 46, 1863–1872 (2001).

[6] Xu M. and Wang L. V., "Universal back-projection algorithm for photoacoustic-computed tomography," Phys. Rev. E 71(1), 016706 (2005).

[7] Jiang H., Yuan Z., and Gu X., "Spatially varying optical and acoustic property reconstruction using finite-element-based photoacoustic tomography," J. Opt. Soc. Am. A, 23, 878-888 (2006).

[8] Paltauf G., Viator J. A., Prahl S. A., Jacques S. L., "Iterative reconstruction algorithm for optoacoustic imaging," J. Acoust. Soc. Am., 112, 1536-1544 (2002).

[9] Siphanto R. I., Thumma K. K., Kolkman R. G. M., van Leeuwen T. G., de Mul F. F. M., van Neck J. W., van Adrichem L. N. A., and Steenbergen W., "Serial noninvasive photoacoustic imaging of neovascularization in tumor angiogenesis," Opt. Express 13, 89–95 (2005).

[10] Laufer J., Delpy D., Elwell C., and Beard P., "Quantitative spatially resolved measurement of tissue chromophore concentrations using photoacoustic spectroscopy: application to the measurement of blood oxygenation and haemoglobin concentration," Phys. Med. Biol., 52, 141–168 (2007).

[11] Razansky D., Vinegoni C., and Ntziachristos V., "Imaging of mesoscopic-scale organisms using selective-plane optoacoustic tomography", Phys. Med. Biol. 54 (9), 2769-2777 (2009).

[12] Wang Y., Xie X., Wang X., Ku G., Gill K. L., ONeal D. P., Stoica G., and Wang L. V., "Photoacoustic tomography of a nanoshell contrast agent in the in vivo rat brain," Nano Lett. 4, 1689-1692 (2004).

[13] Razansky D., Distel M., Vinegoni C., Ma R., Perrimon R., Köster R. W., and Ntziachristos V., "Multi-spectral optoacoustic tomography of deep-seated fluorescent proteins in-vivo", Nature Photonics, 3(7), 412 - 417 (2009).

[14] Wang X., Xu Y., Xu M., Yokoo S., Fry E. S., and Wang L. V., "Photoacoustic tomography of biological tissues with high cross-section resolution: Reconstruction and experiment," Medical Physics 29, 2799–2805 (2002).

[15] Cox B. T., Kara S., Arridge S. R., and Beard P. C., "k-space propagation models for acoustically heterogeneous media: application to biomedical photoacoustics," J. Acoust. Soc. Am., 121, 3453-3464 (2007).

[16] Golub G. H. and van Loan C. F., [Matrix Computations, 3rd Edition], Johns Hopkins Studies in Mathematical Sciences, Baltimore Maryland (1996).